JES

JOURNAL OF
ENVIRONMENTAL
SCIENCES

www.jesc.ac.cn

Decoupling the adsorption mechanisms of arsenate at molecular level on modified cube-shaped sponge loaded superparamagnetic iron oxide nanoparticles

Xiang-Yang Lou [1], Roberto Boada [1,*], Verónica Verdugo [1], Laura Simonelli [2], Gustavo Pérez [1,3], Manuel Valiente [1]

[1] GTS-UAB Research Group, Department of Chemistry, Facultat de Ciències, Universitat Autònoma de Barcelona, 08193 Bellaterra, Spain
[2] ALBA Synchrotron, Carrer de la llum 2-26, Cerdanyola del Vallès, 08290 Barcelona, Spain
[3] Centro de Excelencia en Nanotecnologia, Leitat Chile, Santiago 7500724, Chile

ABSTRACT

In this study, a commercial cube-shaped open-celled cellulose sponge adsorbent was modified by *in-situ* co-precipitation of superparamagnetic iron oxide nanoparticles (SPION) and used to remove As(V) from aqueous solutions. Fe K-edge X-ray absorption spectroscopy (XAS) and TEM identified maghemite as the main iron phase of the SPION nanoparticles with an average size 13 nm. Batch adsorption experiments at 800 mg/L showed a 63% increase of adsorption capacity when loading 2.6 wt.% mass fraction of SPION in the cube-sponge. Experimental determination of the adsorption thermodynamic parameters indicated that the As(V) adsorption on the composite material is a spontaneous and exothermic process. As K-edge XAS results confirmed that the adsorption enhancement on the composite can be attributed to the nanoparticles loaded. In addition, adsorbed As(V) did not get reduced to more toxic As(III) and formed a binuclear corner-sharing complex with SPION. The advantageous cube-shape of the sponge-loaded SPION composite together with its high affinity and good adsorption capacity for As(V), good regeneration capability and the enhanced-diffusion attributed to its open-celled structure make this adsorbent a good candidate for industrial applications.

© 2022 The Research Center for Eco-Environmental Sciences, Chinese Academy of Sciences. Published by Elsevier B.V.
This is an open access article under the CC BY-NC-ND license
(http://creativecommons.org/licenses/by-nc-nd/4.0/)

Introduction

Arsenic (As) is a major concern regarding environmental pollution and human health due to its high toxicity and carcinogenicity. Although natural processes such as soil weathering and volcanic eruptions release As into the environment,

* Corresponding author.
  E-mail: roberto.boada@uab.cat (R. Boada).

anthropogenic activities are the primary source of arsenic pollution (Alam et al., 2019). The world health organization (WHO) establish the maximum discharge level of As at 10 μg/L (Shakya and Ghosh, 2018). Unfortunately, As concentrations higher than 50 μg/L can still be found in drinking water of several countries. As a result, more than 200 million people in the world are exposed to unacceptable levels of As (Castriota et al., 2020).

Although As exists in both organic and inorganic forms in the environment, inorganic forms are more toxic and the more common ones (Liu and Xie, 2021). In water, As is mostly found as oxyanions of trivalent arsenite, As(III), or pentavalent arsenate, As(V) (He et al., 2020). The latter, As(V), is the thermo-dynamically stable form that generally predominates in oxic surface waters.

Among the available methodologies for As removal, adsorption is considered to be the best one for low concentrations, and the most promising one for industrial applications thanks to its fast and easy operation, and the advantage of being environmentally-friendly and cost-effective (Ploychompoo et al., 2020). An ideal adsorbent for water remediation should be non-toxic, possess excellent chemical resistance, have very low solubility in water and, ultimately, offer the possibility to be used in practical applications (e.g. in columns or membrane systems). Many types of adsorbents have been reported, such as biomass, metal oxides (especially iron oxide), fly ash, graphene and graphene oxide (Long et al., 2020). Among all these materials, superparamagnetic iron oxide nanoparticles (SPION) are considered to be one of the most promising adsorbents due to their remarkable features such as small size ($<$ 30 nm), large specific surface area, non-toxic and facile magnetic separation (Bilgic and Cimen, 2021).

Many efforts are being devoted to optimize the design, synthesis, and usage of SPION to improve their structural stability, adsorption capacity, and adsorption selectivity (Bilgic and Cimen, 2021). However, one of the main remaining drawbacks of nanoparticles is their easy aggregation when they are suspended in water. To overcome this issue, nanoparticles have been often loaded on support materials such as sand, fly ash, and biomass (Hosseini Asl et al., 2017). Our previous studies have shown that commercially available open-celled cellulose porous MetalZorb® sponge can be used as a support to effectively decrease the aggregation of SPION (Morillo et al., 2015). In that work, the SPION was synthesized prior to loading them by spray nebulization over powdered sponge. This method generates a homogeneous dispersion of SPION over a very fine powdered sample, but it does not assure a uniform permeation of the SPION into the pores for coarse powder. In addition, this sponge material shows higher As(V) adsorption capacity than other support materials. However, one of the main limitations for industrial application of previously reported works is the use of such composite materials in very fine powdered form. Hence, when used in adsorption columns, they would limit the flow rate of the solution and even clog the column blocking the flow. Besides, the separation of powdered adsorbents from wastewater is a tedious job and requires sophisticated instrumentations that are hardly available in developing countries. This reduces the feasibility of its implementation at those places with serious contamination issues (Kaljurand and Koel, 2011). Therefore, it is necessary to develop new methodologies for synthesizing composite materials in sizes that could be used in column applications.

In this study, we propose to use SPION supported on commercially available cube-shaped open-celled cellulose sponge (hereafter referred to as "sponge-loaded SPION") as a composite material for the removal of As(V) from aqueous solution. The synthesis of the SPION was performed *in-situ* in the presence of the cube-sponge to overcome the drawbacks of the SPION loading obtained by nebulization for adsorbents that are not in powdered form. Here we report the comprehensive characterization of this cube composite adsorbent material, including a comparison of its adsorption performance with recently reported Fe-based adsorbent materials. In addition, exploiting the sensitivity of X-ray absorption spectroscopy to the local coordination environment of the proben As atoms, we have been able to decouple the adsorption occurring at the different components of the composite sorbent. These results have allowed us to get a better understanding of the As(V) adsorption mechanisms. Besides, the regeneration capability of the material was also evaluated by performing several adsorption-desorption cycles and monitoring the variation of the adsorption capacity.

1. Materials and methods

1.1. Materials

All reagents used were of analytical grade and purchased from Sigma-Aldrich (Missouri, USA), Panreac (Barcelona, Spain), Scharlab (Barcelona, Spain) or Honeywell, (Charlotte, USA). The stock aqueous solution of 1000 mg/L As(V) was prepared from sodium arsenate dibasic heptahydrate (Na$_2$HAsO$_4$•7H$_2$O). The pH was adjusted to 3.6 prior to the adsorption experiments to optimize the adsorption in accordance with previous works (Morillo et al., 2015). The pH was adjusted by adding the appropriate amount of hydrogen chloride (HCl) or sodium hydroxide (NaOH).

Cube-shaped MetalZorb® adsorbent was kindly supplied by CleanWay Environmental Partners, Inc. (Portland, USA). The material is an open-celled cellulose sponge (hereafter referred simply as "sponge") which incorporates a water-insoluble polyamide chelating polymer. The sponge contains free available ethyleneamine and iminodiacetate groups that interact with heavy metals ions by ion exchange mechanism and chelation, respectively (Muñoz et al., 2002). The sponge has low impedance of diffusion and it is light in weight. When used in a column, flow rates of three bed volumes per minute can be obtained at hydrostatic pressures only 60 cm above the bed and without any additional pressurization. These properties make this porous material a good candidate for supporting nanoparticles in industrial water remediation applications. Besides, another very important fact to use this specific sponge stands on their industrial production and commercialization for the removal of metal pollutants in contaminated waters. The averaged dimensions of the cube are (length x width x height): 12.8 $\pm$ 1.8 $\times$ 10.1 $\pm$ 1.1 $\times$ 7.3 $\pm$ 1.3 mm. Each cube has an average weight of 0.20 $\pm$ 0.02 g.

1.2. Preparation of cube sponge-loaded SPION

Following the manufacturer's advice, the sponge was pretreated with 1.0 mol/L HCl to remove all possible pre-absorbed cations. This protonates the amino functional groups, which improves the adsorption capacity of the adsorbent. In addition, this activation step facilitates the immobilization of the nanoparticles on the sponge surface. The activation of the as-received sponge was performed in batches of 6 cubes in a 50 mL tube as follow: immersion of the cubes in Milli-Q water for 24 hr, immersion in 1.0 mol/L HCl solution for 4 hr to fully protonate the iminodiacetate groups, rinsing with Milli-Q water until a pH value of 4.0, immersion in HCl solution at pH 2.5 for 2 hr to equilibrate the pH value, and washing 5 times with Milli-Q water to remove the excess of acid solution. Afterwards, the water was decanted, and the cubes were dried in an oven at 50°C for 24 hr.

SPION was synthesized by co-precipitation using an alkaline mixture of iron chloride hexahydrate (FeCl$_3$•6H$_2$O) and ferrous chloride tetrahydrate (FeCl$_2$•4H$_2$O) solution as described elsewhere (Uheida et al., 2006). The synthesis was carried out while bubbling nitrogen gas to avoid SPION oxidization and while stirring at 300 rpm/min to ensure a proper mixing of all the reagents during the synthesis. The loading of SPION in the cube sponge was carried out in-situ as follows: first, 100 mL Milli-Q water was added to 500 mL Erlenmeyer flask, deoxygenated for 30 mins and heated at 40 °C. Then, the Fe(II) and Fe(III) precursors (0.02 and 0.04 mol/L, respectively), and six sponge cubes were added to the solution and leave it stirring for 30 min. Afterwards, 120 mL of 0.5 mol/L NaOH was added to the solution dropwise and the mixture was stirred for an hour to leave enough time for completing the reaction. The resulting composite material was separated by decanting, washed three times with 50 mL deoxygenated Milli-Q water and dried in an oven at 50°C for 24 hr.

To characterize the SPION particles at different depths of the cube material, several cube samples were cut and divided in three parts: surface (1.5 mm from the surface), quarter (1.5–3.0 mm from the surface) and center (remaining part of the cube) as shown in Appendix A **Fig. S1**. These parts account for the 68%, 28% and 4% of the total cube volume, respectively.

1.3. Characterization of sponge-loaded SPION

Fourier transform infrared spectroscopy (FT-IR, Tensor 27, Bruker, USA) measurements were performed to identify the functional groups of SPION, sponge, and sponge-loaded SPION. Scanning electron microscope (SEM, Merlin, Carl Zeiss AG, Germany) images were collected to get information about the morphology of the materials. The morphology and size of the SPION were characterized by Transmission Electron Microscope (TEM, JEM-1400, JEOL, Japan) in a section of the cube composite material. X-ray powder diffraction (XRD, X-Pert, Philips, Netherlands) was carried out to identify the iron oxide phase and the crystallinity of the nanoparticles. X-ray absorption spectroscopy (XAS) measurements at the Fe K-edge were performed at BL22 CLÆSS beamline of ALBA CELLS synchrotron (Simonelli et al., 2016).

1.4. Adsorption experiments

The experiments were performed in batch mode using 50 mL plastic tubes containing 25 mL As(V) solution and one cube of the adsorbent material (sponge or sponge-loaded SPION, 0.20 g). The tubes were agitated mechanically at 300 rpm/min and at 293, 318 or 343 K by using a shaker inside a temperature controlled incubator. The solutions were separated from the adsorbents by filtration and As(V) concentration in the solution was determined by UV–visible spectrometric technique based on the molybdenum blue method (see Appendix A **Section S1**). The adsorption capacity and removal percentage at the equilibrium was calculated by using Eq. (1) and Eq. (2), respectively:

$$q_e = (C_o - C_e)\frac{V}{m} \tag{1}$$

$$\text{Removal percentage} = \frac{(C_o - C_e)}{C_o} \times 100\% \tag{2}$$

where q_e (mg/g) is the adsorption capacity, V (L) is the volume of the arsenic solution, m (g) is the weight of the adsorbent, C_o (mg/L) and C_e (mg/L) are initial and equilibrium concentrations of As(V) solution, respectively.

1.5. Adsorption-desorption cycle experiments

For regenerating the sponge-loaded SPION cube adsorbent material after adsorption (initial concentration 200 mg/L), the cube was separated by filtration, washed three times with Milli-Q water, and immersed in 25 mL 0.5 mol/L NaOH solution to desorb the arsenic. After shaking at 300 rpm for 60 min, the adsorbent was separated by filtration and rinsed with 25 mL Milli-Q water. Finally, the cube sponge-loaded SPION was dried at 50 °C for 24 hr before carrying out the next adsorption run. This adsorption/desorption cycle was repeated five times to determine the regeneration capacity of the composite adsorbent material.

1.6. Characterization of sponge-loaded SPION

The XAS experiments were carried out at BL22 CLÆSS beamline of ALBA CELLS synchrotron (Simonelli et al., 2016). Fe K-edge XAS measurements were collected in transmission mode at room temperature to study the iron oxide phase in both SPION and sponge-loaded SPION. A Si(111) double crystal monochromator. For the sponge-loaded SPION samples, 22 mg of the material was pressed into 5 mm pellets. For SPION samples and Fe reference compounds, 5 mg of SPION was thoroughly mixed with 100 mg of cellulose and pressed into 13 mm pellets.

As K-edge XAS measurements were performed to unravel the chemical state and coordination environment of the adsorbed arsenic after exposing the adsorbents to an initial concentration of 200 mg/L As(V). In order to get information at different depths of both materials, cube sponge and sponge-loaded SPION, the cubes were split in three regions as mentioned before: surface, quarter and center. A Si(311) double crystal monochromator was used. Measurements of the As-sponge, As-sponge-loaded SPION adsorbents and As reference
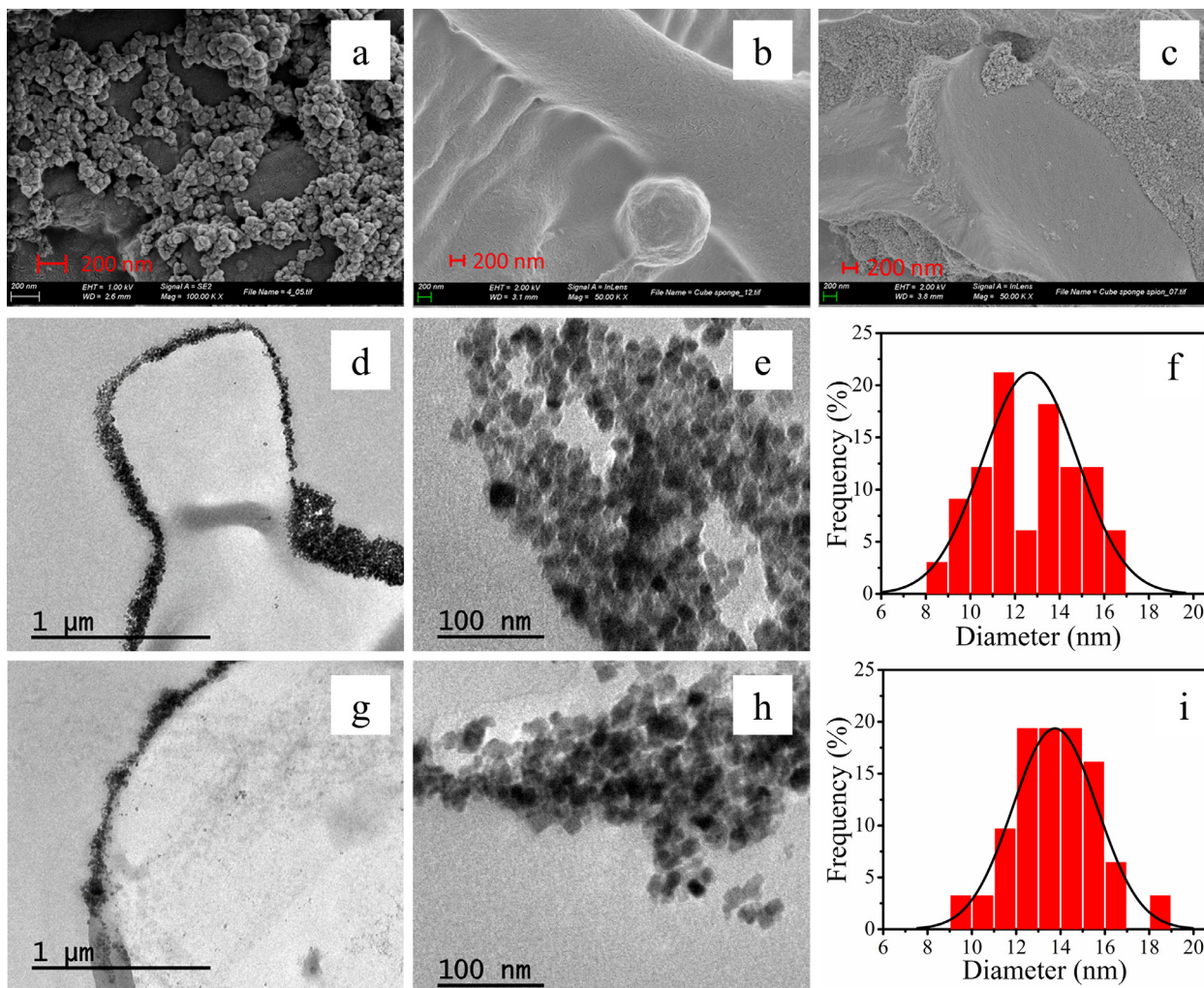
Fig. 1 – SEM images for (a) SPION, (b) sponge, and (c) sponge-loaded SPION. TEM images and particle size histogram for (d, e, f) surface and center (g, h, i) parts of sponge-loaded SPION.

samples were performed in transmission mode using ionization chambers. These samples were milled and pressed into pellets without using any binder. For the As-SPION sample, the spectra was collected in fluorescence mode using a multi-element silicon drift detector with Xspress3 electronics. In this case, to reduce the self-absorption effects, the As-SPION sample was homogeneously mixed with cellulose using a 1:10 ratio. The measurements were carried out at liquid nitrogen temperature to minimize any radiation damage.

XAS data analysis was performed according to standard procedures using ATHENA and ARTEMIS software of the Demeter package (Ravel and Newville, 2005).

2.   Results and discussion

2.1.   Characterization of adsorbent materials

The SEM images (top panels in Fig. 1) revealed the microstructure and morphology of the adsorbent materials. A severe aggregation of the nanoparticles was found for SPION sample,

see Fig. 1a. The open-celled structure of sponge composed by connected pores can be seen in Fig. 1b. The loading of SPION into sponge is clearly indicated by the darkening of the final material with respect to the original sponge (see Appendix A Fig. S2). After loading the nanoparticles, the surface of sponge becomes more heterogeneous, see Fig. 1c. It is clear that having the sponge as support helps in reducing the nanoparticle aggregation to a large extent. SEM images of sponge and sponge-loaded SPION with smaller magnification are also shown in Appendix A Fig. S3.

The TEM images of sponge-loaded SPION and the corresponding particle size distribution histograms calculated using Image-Pro-Plus software (Media Cybernetics, Silver Spring, USA) are shown in Fig. 1 (middle and bottom panels). The nanoparticles are coating the surface of the sponge and they are not blocking the pores, which preserves the advantageous convection properties of the original sponge material. The nanoparticles are mostly spherical, and the mean nanoparticle size found for the surface and the center parts of the cube sponge-loaded SPION were 12.7 and 13.8 nm, respectively. The histogram shows that the particle size dispersion, considering
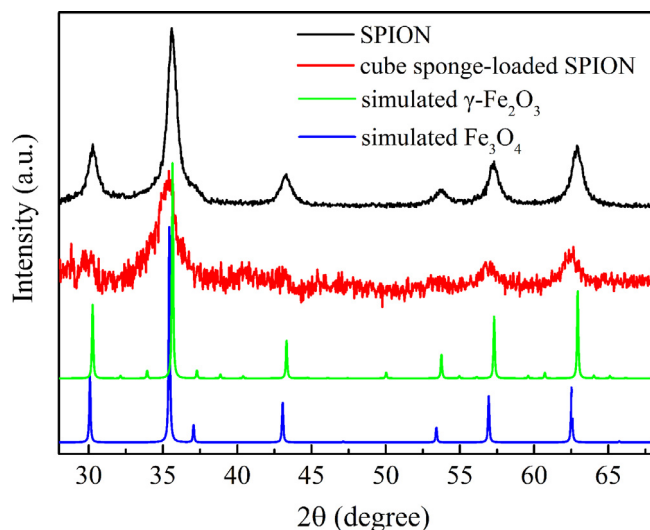
Fig. 2 – XRD spectra of SPION, cube sponge-loaded SPION, simulated γ-Fe₂O₃ and simulated Fe₃O₄.

a normal distribution, has similar width for both, surface and center parts of the cube, see Fig. 1f and Fig. 1i. However, almost a bimodal distribution is found at the surface part which highlights the important contribution of the smaller particles. Indeed, a detailed analysis of the particle size data revealed that, in average, due to the smaller particle size, the surface/volume ratio is 10% larger at the surface part.

XRD was carried out to identify the iron oxide phase of the nanoparticles. Fig. 2 shows the comparison of the experimental diffraction patterns with the simulated ones for Fe₂O₃ (American Mineralogist Crystal Structure Database, code: 0007898) (Barrón et al., 2003) and Fe₃O₄ (American Mineralogist Crystal Structure Database, code: 0002400) (Haavik et al., 2000). The diffraction pattern of both samples displayed the characteristic reflections of the spinel structure; however, it was not possible to determine the iron phase since the diffraction patterns of maghemite, γ-Fe₂O₃, and magnetite, Fe₃O₄, are very similar and the width of the diffraction peaks yield by the nanoparticles were quite wide. In order to further identify the iron oxide phase, XAS analysis at the Fe K-edge was performed. Fig. 3 shows the comparison of the X-ray absorption near edge structure (XANES) region of the Fe K-edge XAS spectra collected on SPION, sponge-loaded SPION (surface) and the reference bulk iron oxide materials, magnetite (Fe₃O₄) and maghemite (γ-Fe₂O₃). Magnetite and maghemite references show a clearly differentiated XANES spectra. The position of the absorption rising edge, which is highly influenced by the oxidation state of the Fe ions, appears at higher energy for maghemite which contains only Fe(III) ions. Indeed, maghemite can be considered as a Fe(II)-deficient magnetite. In addition, the energy shift of the edge is also influenced by the Fe−O bond length (the shorter the interatomic distance, the higher the edge energy) and this can account for bond length expansion in non-stochiometric iron oxide nanoparticles due to the reduced coordination. In our case, the XANES spectrum of SPION is almost identical to the maghemite reference reflecting the bulk character of the nanoparticle aggregates. On the other side, the spectrum of the SPION nanoparticles loaded in the sponge is slightly different from the one of the SPION sample. It also resembles the spectral profile of the maghemite reference, but the spectral features A, B and C are smeared out respect to SPION. Similarly, we found that, when comparing the extracted extended X-ray absorption fine structure (EXAFS) signal for both samples (see inset in Fig. 2b), the amplitude of the oscillation is smaller for sponge-loaded SPION. This is related with the decrease of the coordination number of Fe atoms close to the surface of the iron oxide nanoparticles and the increase of disorder respect to the bulk structure. These observations point out that the main iron phase of the nanoparticles in the sponge-loaded SPION is maghemite, i.e. the Fe oxidation state is dominated by Fe(III). This is beneficial in terms of the adsorption capacity since maghemite provides a higher adsorption capacity and a more stable Fe-As complex after As(V) adsorption than magnetite (Mejia-Santillan et al., 2018). Regarding the different parts of the cube, no significant change in the chemical state of the iron oxide was found at different parts of the cube as shown in Appendix A **Fig. S4**. A rough estimation of the atomic Fe concentration obtained from the absorption jump of the XAS spectrum revealed that there is an average of ∼15% less Fe in the surface part than in the center part. This observation agrees with the smaller particle size and the higher surface/volume ratio of the SPION loaded on the surface part of the cube obtained from TEM. Hence, this corroborates that the particles at the surface part of the cube are smaller respect to the ones at the center.

2.2.   Adsorption performance

To assess the As(V) adsorption performance of cube sponge and cube sponge-loaded SPION, batch adsorption experiments with various initial concentrations, contact times and different temperatures were performed. As seen in Fig. 4a, the adsorption capacity of sponge and sponge-loaded SPION increase when increasing the As(V) initial concentration. Also, both adsorbents show better adsorption at 293 K than at 343 K, while sponge-loaded SPION has a higher adsorption capacity than sponge alone. These adsorption experiments did not reach saturation within the concentration range studied. However, the maximum initial concentration used in this study is 800 mg/L, which is much higher than the concentration found in polluted groundwater (Ali et al., 2019). However, it is worth mentioning that for the lowest As(V) concentration considered for this study (25 mg/L), which is much more relevant for environmental remediation applications, a 98% removal was achieved.

Adsorption results with different contact times, Fig. 4b, revealed that there is a transient initial stage in which the adsorption capacity sharply increases. This can be attributed to the large number of adsorption sites initially available on the surface of the adsorbent. The adsorption capacity becomes almost constant after ∼60 min. When comparing the two different adsorbents studied, sponge-loaded SPION showed a higher equilibrium adsorption capacity and a slightly faster adsorption process.

Our results show that the adsorption capacity of the sponge increases notably after loading SPION. Considering an
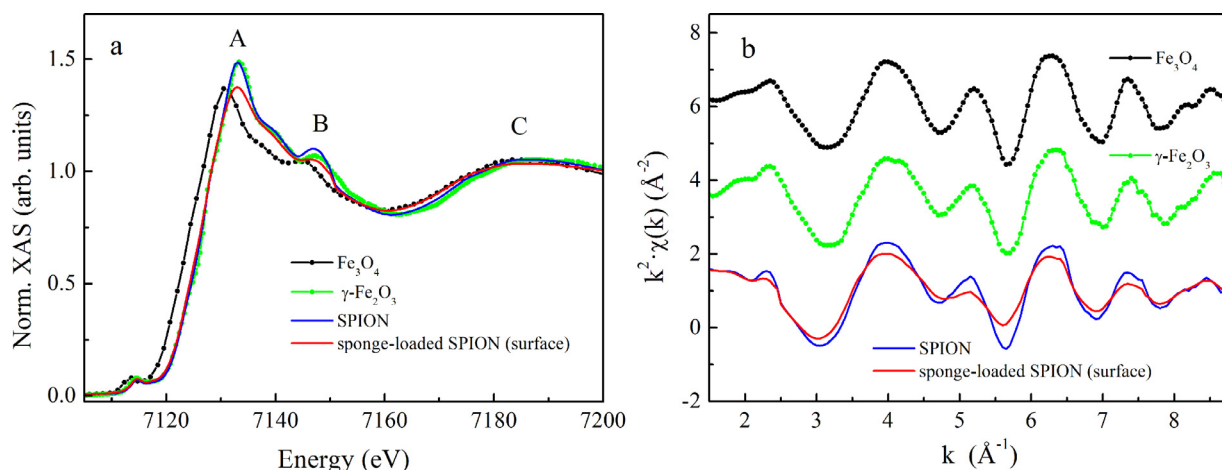
Fig. 3 – Fe K-edge XANES spectra (a) and EXAFS spectra (b) of SPION, sponge-loaded SPION (surface) and the two iron oxide reference materials (Fe₃O₄, γ-Fe₂O₃).
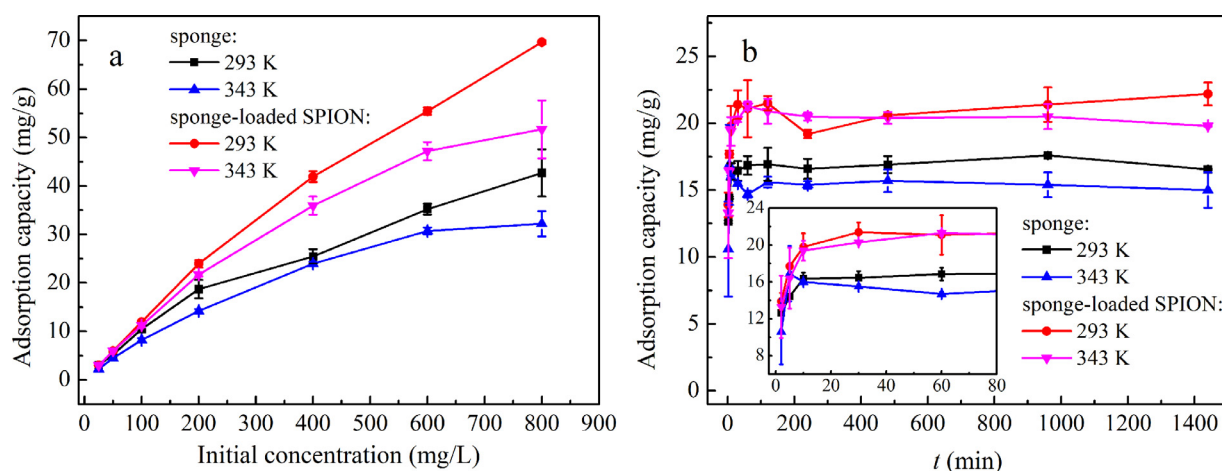

Fig. 4 – As(V) adsorption capacity using cube sponge and sponge-loaded SPION with different (a) initial concentration and (b) contact time.

initial concentration of 200 mg/L and at 293 K, the adsorption capacity increases from 18.7 to 24.0 mg/g after loading SPION. This means that the adsorption capacity of sponge increases 28.3% after loading only 2.6 wt.% mass fraction of SPION (63.2% at 800 mg/L initial concentration). This can be attributed to the high affinity of SPION to As(V) as it has been reported previously (Hao et al., 2018). In fact, this adsorption capacity is considerably higher than the ones reported for other iron-based composite materials, see Table 1. For example, Bakshi and coworkers reported a maximum adsorption capacity of 15.66 mg/g when loading 59.64 wt% zero-valent iron on red oak biochar (particle size < 0.04 mm) (Bakshi et al., 2018). A widely used iron-hydroxide based granulate commercial adsorbent GEH-102 (Fe(OH)₃ and β-FeO(OH), size 300–2000 μm) shows a maximum As(V) adsorption capacity of 25.24 mg/g (Moraga et al., 2019). In our case, the mass fraction of the iron nanoparticulate adsorbent loaded is much lower than in those works, and, in addition, we are not quoting the calculated maximum adsorption capacity as it is usually reported by several authors. In this study, for a maximum initial As(V) con-

centration of 800 mg/L an adsorption capacity of 69.68 mg/g is obtained for sponge-loaded SPION which outperforms those other Fe-based adsorbents.

The independent adsorption performance of SPION supported in the sponge can be assessed when the adsorption capacities of the two materials forming the composite adsorbent are disentangled. When comparing with the adsorption capacity of the SPION sample, 27.7 mg/g, we found that, in proportion, the supported SPION adsorbs ∼8 times more As(V) than the unsupported nanoparticles. This reflects the reduction of the surface area due to the aggregation of the unsupported nanoparticles in the SPION samples as it has been shown above in the SEM images. Indeed, the different behavior of the SPION when loaded in the sponge is also reflected in the temperature variation of the adsorption capacity. For SPION sample, there is a 21.7% adsorption increase when going from 293 to 343 K, whereas the SPION, when loaded on the sponge, displays a larger increase, 38.6%, see Appendix A **Table S1**. This explains why the temperature variation of the whole composite adsorbent decreases less, −9.6%, than the

Table 1 – Comparison of adsorption capacities with similar system.

Support material	Size (mm)	Iron loading (wt.%)	Iron phase	Maximum adsorption capacity (mg/g)	Reference
Cellulose sponge	cube (13×10×7)	1.80	γ-Fe$_2$O$_3$	69.68*	This work
Sponge	half-cylinder (30 Ø x 15)	~12	iron oxide	4.6	(Nguyen et al., 2010)
NONE	0.3-2	52-62	Fe(OH)$_3$; β-FeO(OH)	25.24	(Moraga et al., 2019)
Corn straw biochar	0.5-1	6.05	Fe	6.80	(He et al., 2018)
Activated carbon	0.85	3.5	iron oxyhydroxides	4.96	(Nieto-Delgado et al., 2019)
Red oak biochar	<0.04	59.64	Zero-valent iron	15.66	(Bakshi et al., 2018)
Switchgrass biochar	<0.04	55.72	Zero-valent iron	6.48	(Bakshi et al., 2018)
Clay-activated carbon	2–3	–	iron oxide	5.0	(Pawar et al., 2018)
Fungal biomass	<0.4	–	iron oxide	10.3	(Cárdenas-González et al., 2017)
Darco 20×50	0.3-0.85	4.22	β-FeOOH	1.95	(Chang et al., 2010)

* at 800 mg/L initial concentration.

value that can be estimated when combining the data from the individual components, −22.2%.

22.3. Adsorption isotherm modeling

Adsorption isotherms were performed to understand the adsorption mechanism of cube sponge-loaded SPION. Langmuir, Freundlich, and Temkin, the most used isotherm models, were applied to interpret the experimental data (Tran et al., 2020). Langmuir model assumes that the adsorption occurs on a homogeneous surface and that all binding sites have equal affinity for the adsorbate (Eq. (3)). Freundlich isotherm assumes multilayer adsorption, with non-uniform distribution of adsorption heat and affinities over the heterogeneous surface (Eq. (4)). Temkin isotherm contains a factor that explicitly considers the adsorbent–adsorbate interactions and it is mostly used for electrostatic interaction-based chemical adsorption (Eq. (5)).

Langmuir isotherm model:

$$\frac{1}{q_e} = \left(\frac{1}{K_L q_m}\right)\frac{1}{C_e} + \frac{1}{q_m} \tag{3}$$

Freundlich isotherm model:

$$\log q_e = \log K_F + \frac{1}{n}\log C_e \tag{4}$$

Temkin isotherm model:

$$q_e = \frac{RT}{b_T}\ln A_T + \frac{RT}{b_T}\ln C_e \tag{5}$$

where q_e (mg/g) and q_m (mg/g) are the equilibrium and maximum adsorption capacity, respectively. C_e (mg/g) is the concentration remaining in the solution. K_L (L/mg) is the Langmuir constant, which is related to the pollutant affinity to binding sites. K_F ((mg/g)(L/mg)$^{1/n}$) and n are Freundlich adsorption constants, and $1/n$ gives an indication of the preferential adsorption process. R is the ideal gas constant 8.3145 [J/(mol•K)] and T (K) is the absolute temperature. A_T (L/g) and b_T (kJ/mol) are Temkin constants, which are linked to the maximum binding energy and heat of adsorption, respectively.

The adsorption isotherm data of sponge and sponge-loaded SPION at 293 and 343 K were fitted to these models, see Fig. 5. The results from the fits are displayed in Table 2. A relatively good fit was found for the three models ($R^2 > 0.90$), however, the best model is Freundlich which highlights the importance of the heterogeneous surface of the adsorbents. In Freundlich isotherm model, the values of $1/n$ are less than 1 for both adsorbents which indicates that the As(V) adsorption is favorable in both materials. Besides, significant higher K_F values for the sponge-loaded SPION system at both temperatures means that adsorption capacity increased after loading the nanoparticles.

2.4. Adsorption kinetic studies

Kinetic parameters are important to determine the efficiency and mechanism of the adsorption process that is a key knowledge to scale up the As(V) removal. To study the rate and mechanism of As(V) adsorption onto sponge-loaded SPION, the experimental kinetic data were fitted to the pseudo-first order kinetic model (Eq. (6)) and pseudo-second order kinetic model (Eq. (7)) (Tran et al., 2017):

Pseudo-first order kinetic model:

$$\log(q_e - q_t) = \log q_e - \frac{K_1}{2.303}t \tag{6}$$

Pseudo-second order kinetics model:

$$\frac{t}{q_t} = \frac{1}{K_2 q_e^2} + \frac{t}{q_e} \tag{7}$$

Where, q_e (mg/g) and q_t (mg/g) are the adsorption capacity at equilibrium and at any time t (min), respectively; K_1 and K_2 are the rate constants of each respective model.

Sponge and sponge-loaded SPION adsorption data at 293 and 343 K were fitted to these kinetic models, see Fig. 6. Regression coefficients and rate constants are shown in Table 3. In this case, the regression coefficients of the pseudo-second order model are higher than 0.99 for both sponge and sponge-loaded SPION, while regression coefficients of pseudo-first order were below 0.80. Hence, the adsorption kinetics of both
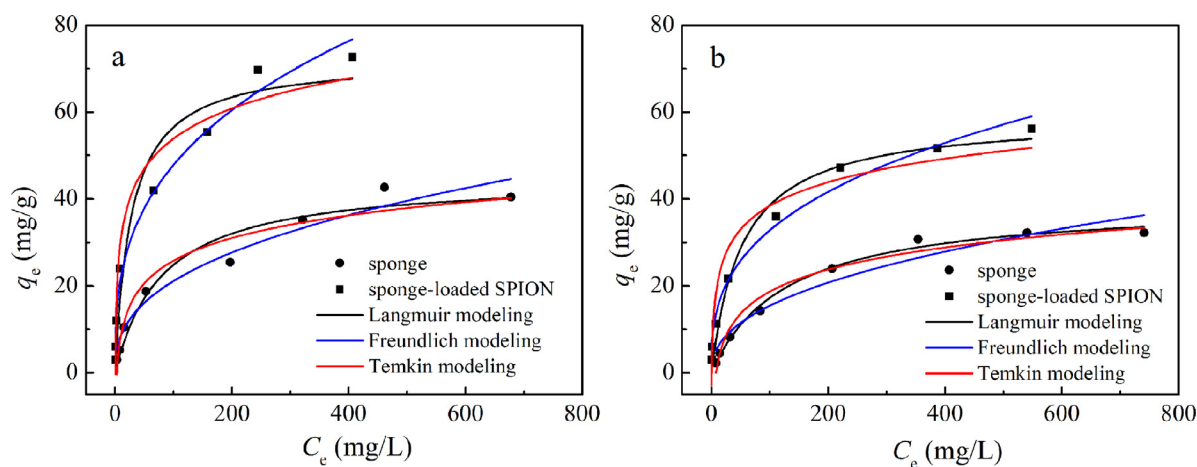
Fig. 5 – Isotherm modeling of As(V) adsorption on sponge and sponge-loaded SPION experimental data. (a) at 293 K and (b) at 343 K.

Table 2 – The parameters of different isotherms models for sponge and sponge-loaded SPION, expressed in the following units: T (K), q_m (mg/g), K_L (L/mg), K_F ((mg/g) (L/mg)$^{1/n}$), A_T (L/g), b_T (kJ/mol).

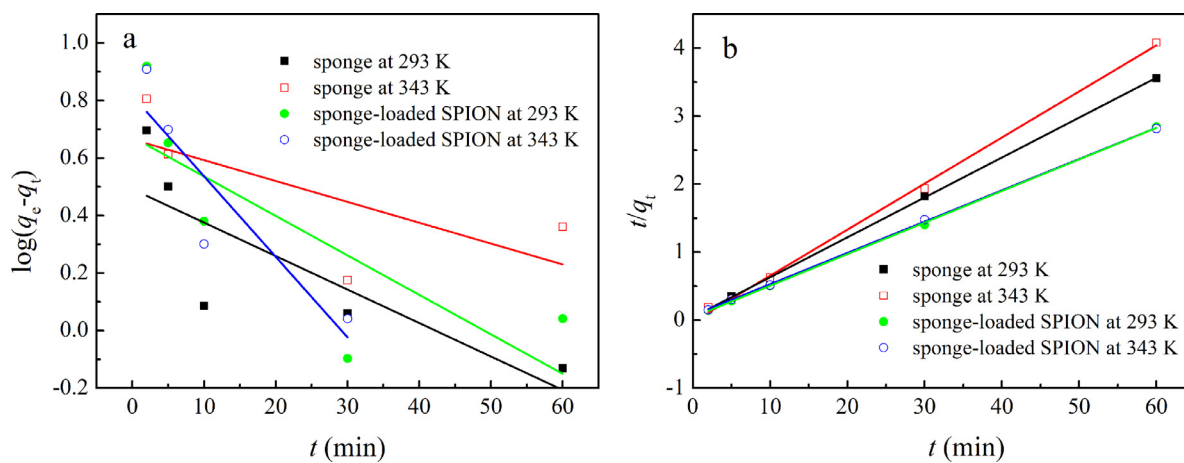| Adsorbents	T	Langmuir isotherm			Freundlich isotherm			Temkin isotherm		
		q_m	K_L	R^2	K_F	$1/n$	R^2	A_T	b_T	R^2
sponge	293	45.00	0.012	0.95	3.49	0.39	0.96	0.31	0.32	0.95
	343	39.36	0.008	0.99	2.16	0.43	0.94	0.13	0.39	0.97
sponge-loaded	293	72.24	0.036	0.94	10.12	0.34	0.98	2.21	0.24	0.96
SPION	343	58.97	0.019	0.98	6.69	0.35	0.98	1.35	0.36	0.93

Fig. 6 – Kinetic modeling of As(V) adsorption on sponge and sponge-loaded SPION at 293 K and 343 K. (a) Pseudo-first order model and (b) Pseudo-second order model.

systems are better described by the pseudo-second order model. Therefore, chemisorption is controlling the speed of the adsorption process. FT-IR results (Appendix A **Fig. S5**) confirm the existence of free available hydroxyl group (-OH), ethyleneamine (-NH$_2$–CH$_2$–CH$_2$-) and iminodiacetate (–(C = O)-NH-(C = O)-) groups in the adsorbents. This implies the influence of ligand exchange and ion exchange mechanisms through the sharing/exchange of electrons between adsorbent functional groups and As(V) during adsorption (Hu et al., 2019; Singh et al., 2012).

The activation energy E_a for adsorption of As(V) onto sponge-loaded SPION can be calculated from the pseudo-second order rate constant, K_2, using the following Arrhenius equation (Eq. (8)) (Lima et al., 2019):

$$\ln K_2 = \ln A - \frac{E_a}{RT} \tag{8}$$

Table 3 – Kinetic parameters for As(V) adsorption onto sponge and sponge-loaded SPION.

Adsorbent	T (K)	Pseudo-first order		Pseudo-second order	
		K_1 (min^{-1})	R^2	K_2 (g/(mg•min))	R^2
sponge	293	0.0268	0.5671	0.0782	0.9999
	343	0.0167	0.2468	0.0929	0.9964
sponge-loaded SPION	293	0.0316	0.4977	0.0519	0.9996
	343	0.0645	0.7299	0.0297	0.9997

Table 4 – Thermodynamic parameters for As(V) adsorption onto sponge and sponge-loaded SPION.

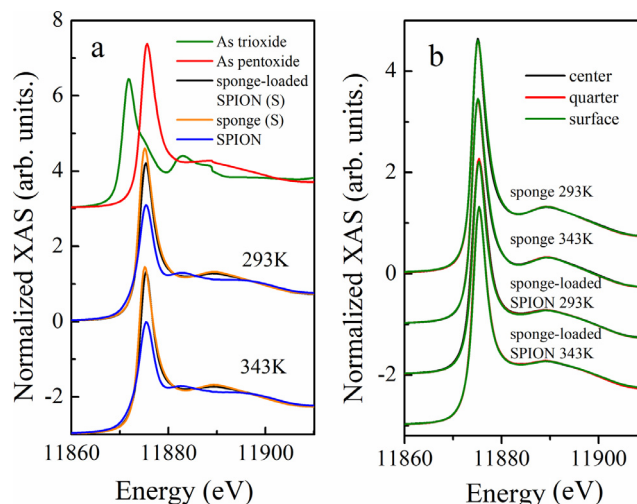| Adsorbent	T(K)	ΔG^o(kJ/mol)	ΔH^o(kJ/mol)	ΔS^o(J/mol)
sponge	293	−14.22	−12.30	6.56
	318	−14.39		
	343	−14.55		
sponge-loaded SPION	293	−19.28	−22.80	−12.02
	318	−18.98		
	343	−18.68		

Fig. 7 – As K-edge XANES spectra: (a) compare of the spectra collected on the adsorbent materials with the As reference compounds and (b) compare of the spectra collected on the different parts of cube sponge and sponge-loaded SPION.

where K_2 is the adsorption rate constant, A is the Arrhenius constant, R is the ideal gas constant 8.3145 (J/(mol•K)) and T (K) is the absolute temperature. The E_a values obtained for sponge and sponge-loaded SPION were 9.86 and 17.69 kJ/mol, respectively. This indicates that sponge-loaded SPION shows higher dominance of chemical adsorption than original sponge.

2.5. Thermodynamics analysis

Thermodynamic parameters such as Gibbs' free energy change (ΔG^o), enthalpy change (ΔH^o) and entropy change (ΔS^o) can predict the feasibility and nature of the adsorption process (Lima et al., 2019). The Gibbs free energy of adsorption can be expressed as (Eq. (9)):

$$\Delta G^o = -RT \ln K^o \tag{9}$$

where, K^o is the standard distribution coefficient of the adsorption (Eq. (10)):

$$K^o = \frac{q_e}{q^o} / \frac{C_e}{C^o} \tag{10}$$

where, q^o and C^o and are the standard states of solution in solid and liquid, respectively. Here, q^o is selected as 1 mol/kg, and C^o is selected as 1 mol/L.

ΔG^o is also related to ΔS^o and ΔH^o as follow (Eq. (11)):

$$\Delta G^o = \Delta H^o - T\Delta S^o \tag{11}$$

By constructing a plot of lnK^o versus 1/T, ΔS^o can be calculated from the intercept and ΔH^o can be obtained from the slope. The results are displayed in Table 4 and Appendix A **Fig. S6**.

The negative ΔG^o values obtained for sponge and sponge-loaded SPION at three temperatures indicate that the adsorption of As(V) onto both adsorbent materials is spontaneous.

Values of ΔH^o are −12.30 and −22.80 kJ/mol for sponge and sponge-loaded SPION respectively, which indicates the As(V) adsorption on these two adsorbents is an exothermic process. The loading of 2.6 wt.% SPION on sponge did not change the exothermic nature of As(V) adsorption on the sponge, although the adsorption on iron oxide is an endothermic process as previously reported (Liu et al., 2015). The spontaneous and exothermic nature of As(V) adsorption imply that adsorption of As(V) on the adsorbents is favorable, which agrees with the results obtained from fitting of Freundlich model.

2.6. Chemical state and coordination environment of adsorbed As

Although the study of the macroscopic adsorption behavior and the thermodynamic calculations provides some evidence that the arsenic is chemically adsorbed on sponge and sponge-loaded SPION, information about the oxidation state and coordination environment of As after being adsorbed is still missing. As K-edge XAS measurements were performed to get a better insight of the adsorption process at the molecular scale.

Fig. 7a displays the As K-edge XANES spectra collected on the adsorbent materials and the As reference compounds (arsenic trioxide, As(III); and arsenic pentoxide, As(V)). These two As reference compounds display a markedly different spectral profile. The pentoxide is shifted 3.7 eV towards higher energy respect to the trioxide. Thus, the white-line feature (first resonance after the rising absorption edge) appears at 11,875.5 and 11,871.7 eV for pentoxide and trioxide, respectively. The direct comparison of the spectra collected on the adsorbent samples with the As reference compounds reveals that the arsenic adsorbed in the materials remains as As(V). Hence, no major redox reaction occurred upon As(V) adsorption on any of the materials. The spectral feature after the white line appears at different energy for sponge and SPION reflecting the
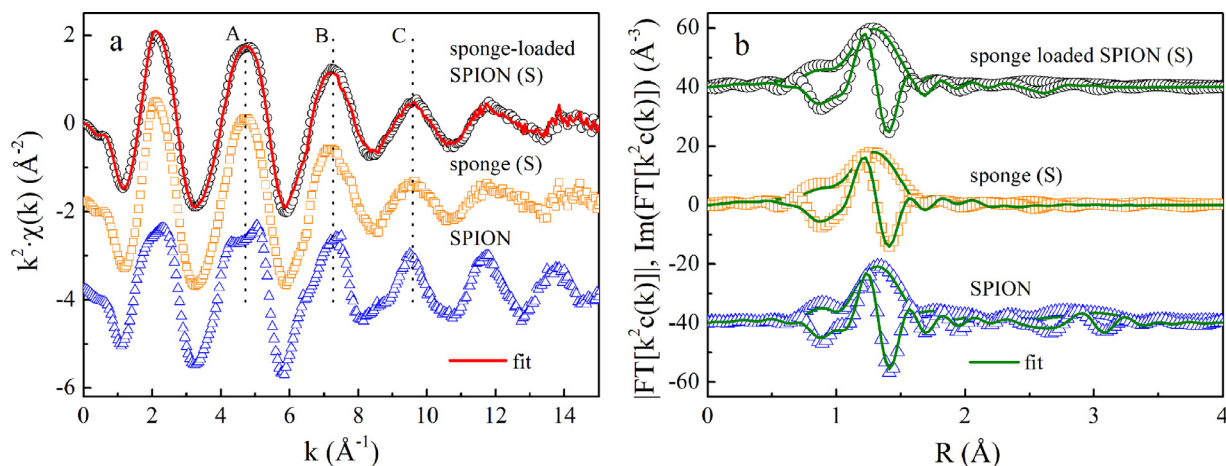
Fig. 8 – As K-edge EXAFS spectra: (a) EXAFS spectra for adsorbents after As(V) adsorption at 293 K and results of the linear combination fitting analysis for surface part of sponge-loaded SPION (line); (b) Pseudo-radial distribution function for adsorbents after As(V) adsorption at 293 K (symbols are experimental data and lines are fits).

different coordination environment of As(V) in the two adsorbents. As expected, the spectrum for the composite adsorbent sample, sponge-loaded SPION, lies in between the two, being more similar to sponge due to the low loading of nanoparticles. As shown in Fig. 7b, the XANES spectra does not remarkably change when increasing the adsorption temperature from 293 to 343 K, therefore, the temperature does not affect relevantly the oxidation state of the adsorbed As. In addition, no change in the oxidation state of the adsorbed As was found as a function of the penetration depth of the cube neither in sponge nor in sponge-loaded SPION, see Fig. 7b. Hence, the same adsorption process occurs at the different parts of the cube due to the good diffusion properties of the sponge material and the rather homogeneity of the composite adsorbent material.

The different local coordination environment of As in SPION and sponge adsorbents is more evident when representing the EXAFS signal and the pseudo-radial distribution function, see Fig. 8. SPION displays a more structured EXAFS signal than sponge. As can be seen Fig. 8a, for SPION, feature A from sponge is double, and features B and C are sharper and have a shoulder at lower k, whereas those features are much simpler and smoother in the case of sponge. As expected, the EXAFS for the sponge-loaded SPION is similar to the one for sponge, but it has some resemblance to SPION as can be noticed by the slight flattening of feature A and the change in shape of features B and C. A semi-quantitative analysis of the ratio between the two components, sponge and SPION, in the sponge-loaded SPION sample can be obtained from the linear combination fitting analysis of the EXAFS signal. The results show that, at 293 K, around 21% of As(V) is adsorbed into the loaded nanoparticles (Fig. 8a and Appendix A Fig. S7a), whereas this amount increases to 42% at 343 K (Appendix A Fig. S7b). These results are in good agreement with those obtained from the adsorption data reported above and confirm that the As(V) adsorbed on the loaded nanoparticles increases when increasing the temperature. In addition, no change was

found in Fe K-edge XAS spectra after adsorption As for SPION and sponge-loaded SPION samples.

The Fourier-transformed spectra in R-space, see Fig. 8b, is dominated by the As−O first-neighbor contribution. The modelling of the EXAFS signals revealed that the As-O bond distance in sponge and SPION are 1.69 and 1.70 Å, respectively (Appendix A **Section S12** for further details about the EXAFS modelling). In addition, for SPION and sponge-loaded SPION, there are relatively weak features beyond the first coordination shell that can be attributed to the As−Fe contributions. The different arrangements of the As(V) tetrahedron with the surface of the iron oxide nanoparticle are related to the arsenic surface coverage (van Genuchten et al., 2020). Among all, binuclear corner-sharing, ^{2}C, is found to be the dominant configuration, because it is strongly favored thermodynamically and kinetically, and it is also the most energetically stable. Some authors have reported the presence of the mononuclear corner-sharing, ^{1}V, when arsenic has a relatively low surface coverage, but we can exclude this possibility in the present case since no contribution appears in the pseudo-radial distribution function and, in our study, the high initial concentration of arsenic (200 mg/L) and the good affinity of SPION for As(V) results in a high surface coverage. In that sense, the mononuclear edge-sharing configuration, ^{2}E, is reported to be present in some cases with the high arsenic surface coverage. However, our fitting results are compatible with a dominant contribution of the ^{2}C configuration (see Table 5). In this case, two of the four As–O bonding structures are complexed to Fe atoms (i.e., As–O–Fe) by corner-sharing with the FeO$_6$ octahedron and the remaining two As atoms are present either both as unprotonated As–O or one as unprotonated As–O and the other one as protonated As–O–H (Zhao and Guo, 2014). Despite the differences regarding particle aggregation, both SPION and sponge-loaded SPION samples are composed by maghemite, thus, the coordination on the composite will follow similar trend as in the case of the unsupported nanoparticles.

Table 5 – EXAFS fitting results of SPION, sponge (S) and loaded (S) at 293 K.

Sample	Atomic Pairs	S_0^2	CN	R (Å)	σ^2 (Å²)	ΔE_0 (eV)	R-factor
SPION	As-O	0.85	4	1.70 (0.02)	0.001 (0.0005)	5.7	0.031
	As-O-O		12	$1.82^*(R_{\text{As-O}}) = 3.10$	σ^2(As-O)	(1.1)	
	As-Fe		2	3.39 (0.04)	0.004 (0.003)		
sponge (S)	As-O	1.1	4	1.69 (0.01)	0.003 (0.001)	5.4 (1.8)	0.009
sponge-loaded SPION (S)	As-O	1.1	4	1.69 (0.01)	0.004 (0.002)	5.9 (2.0)	0.010
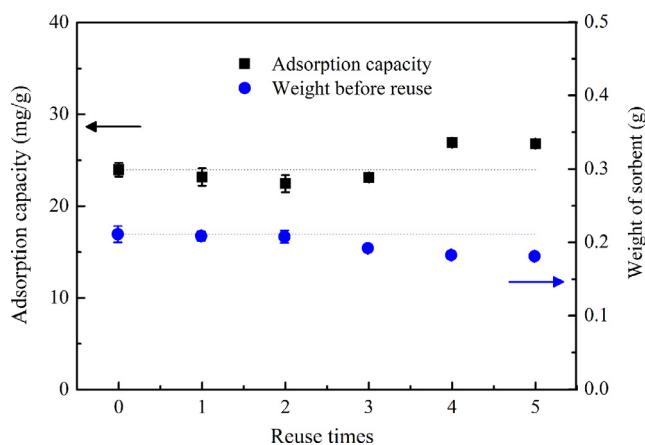
Fig. 9 – Adsorption capacity and weight of adsorbent in different regeneration cycles.

2.7. Regeneration of adsorption materials

To assess the regeneration capacity of cube sponge-loaded SPION, several cycles of adsorption and desorption experiments were performed. As shown in Fig. 9, the adsorption capacity of the adsorbent did not show a significant decrease. Hence, the cube adsorbent maintains a high adsorption capacity even after five adsorption/desorption cycles. The slight increase observed for the fourth and fifth cycles, can be ascribed to the loose powder which broke off from the sponge-loaded SPION during shaking which contributes to the increase of the effective As adsorption from the solution. Besides its good regeneration capabilities, one of the main benefits of this composite adsorbent is that, after its life-time span, it could be easily compressed into a very small volume which hugely facilitates its transport and ultimately waste disposal.

3. Conclusions

In this study, the composite material cube-shaped open-celled cellulose sponge loaded superparamagnetic iron oxide nanoparticles (SPION) was successfully synthesized by the in-situ co-precipitation method and used to remove As(V) from aqueous solution. The adsorption capacity of sponge had a 63.2% enhancement after loading 2.6 wt.% of SPION (maghemite) reaching 69.68 mg/g at 800 mg/L initial As(V) concentration. This value is higher than the maximum adsorption capacity reported for other Fe-based adsorbents.

The isotherm and kinetic modelling indicate a multilayer and heterogeneous adsorption process in which the chemical adsorption is the controlling step. The results from the thermodynamic analysis indicate that the As(V) adsorption on composite material is a spontaneous and exothermic process. In addition, we observed that As(V) was not reduced to more toxic As(III) after being adsorbed, which is desirable for the treatment of As(V) contaminated waters. The modeling of the EXAFS signals revealed that the binuclear corner-sharing configuration, ^{2}C, dominates the As(V) adsorption on SPION. Moreover, we have shown that the cube-shaped sponge-loaded SPION has good regenerative capability and can be used over several adsorption/desorption cycles. In brief, this cube sponge-loaded SPION combines the advantages of both SPION (high affinity, good adsorption capacity) and cube commercial sponge (cheap, open-celled structure and favorable cube-shape) which makes it a promising material for industrial applications.

Appendix A Supplementary data

Supplementary material associated with this article can be found, in the online version, at doi:10.1016/j.jes.2021.09.001.

REFERENCES

Alam, M.Z., Hoque, M.A., Ahammed, G.J., McGee, R., Carpenter-Boggs, L., 2019. Arsenic accumulation in lentil (Lens culinaris) genotypes and risk associated with the consumption of grains. Sci. Rep. 9, 9431.

Ali, W., Rasool, A., Junaid, M., Zhang, H., 2019. A comprehensive review on current status, mechanism, and possible sources of arsenic contamination in groundwater: a global perspective with prominence of Pakistan scenario. Environ. Geochem. Health 41, 737–760.

Bakshi, S., Banik, C., Rathke, S.J., Laird, D.A., 2018. Arsenic sorption on zero-valent iron-biochar complexes. Water Res. 137, 153–163.

Barrón, V., Torrent, J., De Grave, E., 2003. Hydromaghemite, an intermediate in the hydrothermal transformation of 2-line ferrihydrite into hematite. Am. Mineral. 88, 1679–1688.

Bilgic, A., Cimen, A., 2021. Synthesis, characterisation, adsorption studies and comparison of superparamagnetic iron oxide nanoparticles (SPION) with three different amine groups functionalised with BODIPY for the removal of Cr(VI) metal ions from aqueous solutions. Int. J. Environ. Anal. Chem. 1–26.

Cárdenas-González, J.F., Acosta-Rodríguez, I., Téran-Figueroa, Y., Rodríguez-Pérez, A.S., 2017. Bioremoval of arsenic (V) from aqueous solutions by chemically modified fungal biomass. 3 Biotech 7, 226.

Castriota, F., Zushin, P.J.H., Sanchez, S.S., Phillips, R.V., Hubbard, A., Stahl, A., et al., 2020. Chronic arsenic exposure impairs adaptive thermogenesis in male C57BL/6 J mice. Am. J. Physiol. - Endocrinol. Metab. 318, E667–E677.

Chang, Q., Lin, W., Ying, W.C., 2010. Preparation of iron-impregnated granular activated carbon for arsenic removal from drinking water. J. Hazard. Mater. 184, 515–522.

Haavik, C., Stølen, S., Fjellvåg, H., Hanfland, M., Häusermann, D., 2000. Equation of state of magnetite and its high-pressure modification: Thermodynamics of the Fe-O system at high pressure. Am. Mineral. 85, 514–523.

Hao, L., Liu, M., Wang, N., Li, G., 2018. A critical review on arsenic removal from water using iron-based adsorbents. RSC Adv 8, 39545–39560.

He, R., Peng, Z., Lyu, H., Huang, H., Nan, Q., Tang, J., 2018. Synthesis and characterization of an iron-impregnated biochar for aqueous arsenic removal. Sci. Total Environ. 612, 1177–1186.

He, X., Li, Y., Yang, C., Lu, L., Nie, Y., Tian, X., 2020. Carbon dots-MnO2nanocomposites for As(iii) detection in groundwater with high sensitivity and selectivity. Anal. Methods 12, 5572–5580.

Hosseini Asl, S.M., Masomi, M., Hosseini, M., Javadian, H., Ruiz, M., Sastre, A.M., 2017. Synthesis of hydrous iron oxide/aluminum hydroxide composite loaded on coal fly ash as an effective mesoporous and low-cost sorbent for Cr(VI) sorption: Fuzzy logic modeling. Process Saf. Environ. Prot. 107, 153–167.

Hu, X., Jia, L., Cheng, J., Sun, Z., 2019. Magnetic ordered mesoporous carbon materials for adsorption of minocycline from aqueous solution: Preparation, characterization and adsorption mechanism. J. Hazard. Mater. 362, 1–8.

Kaljurand, M., Koel, M., 2011. Recent advancements on greening analytical separation. Crit. Rev. Anal. Chem. 41, 2–20.

Lima, E.C., Hosseini-Bandegharaei, A., Moreno-Piraján, J.C., Anastopoulos, I., 2019. A critical review of the estimation of the thermodynamic parameters on adsorption equilibria. Wrong use of equilibrium constant in the Van't Hoof equation for calculation of thermodynamic parameters of adsorption. J. Mol. Liq. 273, 425–434.

Liu, C., Xie, F., 2021. Highly efficient removal of As(III) by Fe-Mn-Ca composites with the synergistic effect of oxidation and adsorption. Sci. Total Environ. 777, 145289.

Liu, C.H., Chuang, Y.H., Chen, T.Y., Tian, Y., Li, H., Wang, M.K., et al., 2015. Mechanism of Arsenic Adsorption on Magnetite Nanoparticles from Water: Thermodynamic and Spectroscopic Studies. Environ. Sci. Technol. 49, 7726–7734.

Long, X., Wang, X., Guo, X., He, M., 2020. A review of removal technology for antimony in aqueous solution. J. Environ. Sci. 90, 189–204.

Mejia-Santillan, M.E., Pariona, N., Bravo-C, J., Herrera-Trejo, M., Montejo-Alvaro, F., Zarate, A., et al., 2018. Physical and arsenic adsorption properties of maghemite and magnetite sub-microparticles. J. Magn. Magn. Mater. 451, 594–601.

Moraga, B., Toledo, L., Jelínek, L., Yañez, J., Rivas, B.L., Urbano, B.F., 2019. Copolymer–hydrous zirconium oxide hybrid microspheres for arsenic sorption. Water Res 166, 115044.

Morillo, D., Pérez, G., Valiente, M., 2015. Efficient arsenic(V) and arsenic(III) removal from acidic solutions with Novel Forager Sponge-loaded superparamagnetic iron oxide nanoparticles. J. Colloid Interface Sci. 453, 132–141.

Muñoz, J.A., Gonzalo, A., Valiente, M., 2002. Arsenic adsorption by Fe(III)-loaded open-celled cellulose sponge. Thermodynamic and selectivity aspects. Environ. Sci. Technol. 36, 3405–3411.

Nguyen, T.V., Vigneswaran, S., Ngo, H.H., Kandasamy, J., 2010. Arsenic removal by iron oxide coated sponge: Experimental performance and mathematical models. J. Hazard. Mater. 182, 723–729.

Nieto-Delgado, C., Gutiérrez-Martínez, J., Rangel-Méndez, J.R., 2019. Modified activated carbon with interconnected fibrils of iron-oxyhydroxides using Mn^{2+} as morphology regulator, for a superior arsenic removal from water. J. Environ. Sci. 76, 403–414.

Pawar, R.R., Lalhmunsiama, Kim, M., Kim, J.G., Hong, S.M., Sawant, S.Y., Lee, S.M., 2018. Efficient removal of hazardous lead, cadmium, and arsenic from aqueous environment by iron oxide modified clay-activated carbon composite beads. Appl. Clay Sci. 162, 339–350.

Ploychompoo, S., Chen, J., Luo, H., Liang, Q., 2020. Fast and efficient aqueous arsenic removal by functionalized MIL-100(Fe)/rGO/δ-MnO2 ternary composites: Adsorption performance and mechanism. J. Environ. Sci. 91, 22–34.

Ravel, B., Newville, M., 2005. ATHENA, ARTEMIS, HEPHAESTUS: Data analysis for X-ray absorption spectroscopy using IFEFFIT. J. Synchrotron Radiat. 12, 537–541.

Shakya, A.K., Ghosh, P.K., 2018. Simultaneous removal of arsenic, iron and nitrate in an attached growth bioreactor to meet drinking water standards: Importance of sulphate and empty bed contact time. J. Clean. Prod. 186, 1011–1020.

Simonelli, L., Marini, C., Olszewski, W., Ávila Pérez, M., Ramanan, N., Guilera, G., et al., 2016. CLÆSS: The hard X-ray absorption beamline of the ALBA CELLS synchrotron. Cogent Phys 3, 1231987.

Singh, S.K., Townsend, T.G., Mazyck, D., Boyer, T.H., 2012. Equilibrium and intra-particle diffusion of stabilized landfill leachate onto micro- and meso-porous activated carbon. Water Res 46, 491–499.

Tran, H.N., You, S.J., Hosseini-Bandegharaei, A., Chao, H.P., 2017. Mistakes and inconsistencies regarding adsorption of contaminants from aqueous solutions: A critical review. Water Res 120, 88–116.

Tran, T.Van, Nguyen, D.T.C., Le, H.T.N., Vo, D.-V.N., Nanda, S., Nguyen, T.D., 2020. Optimization, equilibrium, adsorption behavior and role of surface functional groups on graphene oxide-based nanocomposite towards diclofenac drug. J. Environ. Sci. 93, 137–150.

Uheida, A., Salazar-Alvarez, G., Björkman, E., Yu, Z., Muhammed, M., 2006. Fe3O4 and γ-Fe2O3 nanoparticles for the adsorption of Co2+ from aqueous solution. J. Colloid Interface Sci. 298, 501–507.

van Genuchten, C.M., Behrends, T., Stipp, S.L.S., Dideriksen, K., 2020. Achieving arsenic concentrations of <1 μg/L by Fe(0) electrolysis: The exceptional performance of magnetite. Water Res 168, 115170.

Zhao, K., Guo, H., 2014. Behavior and mechanism of arsenate adsorption on activated natural siderite: evidences from FTIR and XANES analysis. Environ. Sci. Pollut. Res. 21, 1944–1953.